



ELSEVIER

Mechanics of Materials 32 (2000) 277–301

**MECHANICS
OF
MATERIALS**

www.elsevier.com/locate/mechmat

Finite element analysis of the stress distributions near damaged Si particle clusters in cast Al–Si alloys

Ken Gall ^{a,*}, Mark Horstemeyer ^a, David L. McDowell ^b, Jinghong Fan ^b

^a *Materials and Engineering Sciences Center, Solid and Material Mechanics Department, Sandia National Laboratories, 7011 East Avenue, MS 9405, Livermore, CA 94550, USA*

^b *GWV School of Mechanical Engineering, Georgia Institute of Technology, Atlanta, GA 30332, USA*

Received 12 April 1999; received in revised form 24 September 1999

Abstract

The finite element method is used to study the effects of particle cluster morphology on the fracture and debonding of silicon particles embedded in an Al–1%Si matrix subjected to tensile-compressive cyclic loading conditions. Representative of an actual cast Al–Si alloy, clusters of silicon inclusions (4–8 particles) are considered rather than a single isolated inclusion or an infinite periodic array of inclusions. The silicon particles are modeled with a linear-elastic constitutive relationship and the matrix material is modeled using an internal state variable cyclic plasticity model fitted to experimental data on matrix material. A total of seven parameters are varied to create 16 idealized microstructures: relative particle size, shape, spacing, configuration, alignment, grouping and matrix microporosity. A two-level design of experiment (DOE) methodology is used to screen the relative importance of the seven parameters on the fracture and debonding of the silicon particles. The results of the study demonstrate that particle shape and alignment are undoubtedly the most dominant parameters influencing initial particle fracture and debonding. Particle debonding results in a local intensification of stresses in the Al–1%Si matrix that is significantly larger than that due to particle fracture. The local stress fields after particle fracture are primarily concentrated within the broken particle halves. After the fracture of several particles within a cluster, the spacing between adjacent particles enters as a second-order effect. When several particles within a cluster debond, the spacing between adjacent particles enters as a dominant effect due to the large local stress intensification in the surrounding Al–1%Si matrix. © 2000 Elsevier Science Ltd. All rights reserved.

1. Introduction

Cast Al–Si alloys contain large concentrations of silicon (7–12%) to facilitate the production of high quality castings. Silicon dramatically increases the fluidity of molten Al, improving the hot tear resistance and the feeding behavior of the casting (Kearney and Rooy, 1990). During the solidification of the eutectic Al–Si phase, relatively large silicon particles are formed within an Al–1%Si phase. Particles contained within aluminum alloys are generally classified according to their size (Davidson and Lankford, 1985): precipitates ($d < 0.02 \mu\text{m}$), dispersoids ($0.02 < d < 0.5 \mu\text{m}$), and inclusions ($d > 1 \mu\text{m}$). The silicon particles

* Corresponding author. Tel.: +1-925-294-4546.

E-mail address: kagall@sandia.gov (K. Gall).

in cast Al–Si alloys are considered inclusions since their average size is around 5 μm (Dighe and Gokhale, 1997). It is well established that hard second phase particles dispersed throughout a ductile matrix have a strong influence on the overall ductility (Broek, 1973), fracture toughness (Hahn and Rosenfield, 1975), and fatigue resistance (Broek, 1969) of aluminum alloys. Under monotonic loading, the fracture and debonding of silicon particles (inclusions) leads to the nucleation, growth, and coalescence of voids (Garrison and Moody, 1987; Voigt and Bye, 1991; Samuel and Samuel, 1995). Consequently, the failure of cast aluminum alloys under monotonic loading is very sensitive to the silicon particle morphology. In general, coarse irregular shaped silicon particles promote rapid damage evolution and result in a cast aluminum alloy with low ductility and ultimate tensile strength (Closset and Gruzleski, 1982; Pan et al., 1991; Voigt and Bye, 1991; Samuel and Samuel, 1995; Caceres et al., 1995; Dighe and Gokhale, 1997). Other factors such as high porosity (Samuel and Samuel, 1995) and brittle intermetallics (Murali et al., 1996; Tan et al., 1995; Gall et al., 1999a) can also degrade the monotonic properties of Al–Si castings by further facilitating the localization of damage.

Under cyclic loading conditions, the silicon particles in the eutectic have two potential influences on the fatigue response of cast Al–Si alloys. If the maximum internal defect (oxide or pore) size is small ($\ll 100 \mu\text{m}$), then silicon particles can serve as crack nucleation sites. For example, in squeeze cast Al–Si alloys with silicon concentrations ranging from 7% to 12%, fatigue cracks have been observed to nucleate at silicon particle clusters (Plumtree and Schafer, 1986) or large silicon particles (Shiozawa et al., 1997). In these situations, the damage of silicon particles will have a strong influence on the high cycle fatigue life of cast Al–Si alloys. For example, at low fatigue crack tip driving forces, silicon particles act as barriers to fatigue crack propagation since the cracks are forced to gradually debond the particles and grow through a torturous crack path (Gall et al., 1999b). Hence, the silicon particle morphology has a strong influence on the growth rate of small fatigue cracks over much of the life for high cycle fatigue loading conditions. If the maximum internal defect size is large ($\gg 100 \mu\text{m}$), or the cast component contains external notches with considerable stress concentrations, the silicon particles will have a direct influence on the propagation rate of long fatigue cracks. Cracks nucleated from large defects can be modeled using a modified Paris crack growth law (Ting and Lawrence, 1993). Moreover, cracks growing in the Paris law regime have a crack tip driving force strong enough to fracture a statistically significant number of silicon particles near the crack tip (Gall et al., 1999a,b). The long crack will then subsequently propagate through the damaged silicon particles in the eutectic regions (Gall et al., 1999a,b). Consequently, the growth rate of long cracks is significantly influenced by the silicon particle morphology through differences in the fracture characteristics of the particles (Hoskin et al., 1988; Lee et al., 1995a,b). Finally, the damage associated with silicon particles has also been shown to affect the Bauschinger effect in cast Al–Si alloys subjected to cyclic loading (Horstemeyer, 1998).

Despite the strong influence of the silicon particles on the evolution of damage under monotonic and cyclic loading conditions, the fracture and debonding characteristics of such inclusions is only quantified for idealized particle configurations and geometries (Gurland and Plateau, 1963; Needleman, 1987; Yeh and Liu, 1996). It is still necessary to quantify the relative influence of more realistic microstructural parameters on the fracture and debonding of silicon particles embedded in an aluminum matrix. Previous metallurgical investigations (Gurland and Plateau, 1963; Yeh and Liu, 1996) have shown that the fracture of silicon particles embedded in an aluminum matrix is linked to dislocation motion in the Al. The latter study (Yeh and Liu, 1996) further asserted that continuum theory was unable predict the proper dependence of the volume fraction of fractured particles on the applied stress and plastic strain levels. The particle fracture hypothesis was based on the observation that cast materials with drastically different aluminum matrix yield strengths experienced silicon particle fracture at similar levels of macroscopic plastic deformation. Consequently, Yeh and Liu (1996) concluded that the fracture process was only dictated by the impingement of dislocations on the particles as caused by large scale yielding in the specimens, and that a continuum analysis could not capture such an effect. However, the conclusion by Yeh and Liu (1996) was

not based on a thorough knowledge of the stress and strain distributions predicted by considering a material containing inclusions that is undergoing plastic flow in the matrix. From a continuum standpoint, the onset of plastic flow in the matrix is also accompanied by sharp increases of the stress in the silicon particle as the elastic inclusion attempts to maintain compatibility with the flowing matrix. In addition, continuum theory predicts trends in particle fracture that are not easily captured with dislocation-based models, as will be further discussed.

A proposed micro-mechanical model based on dislocation pileups (Yeh and Liu, 1996) captured the overall dependence of the volume fraction of fractured silicon particles on the applied stress and strain. However, despite the fact that particle shape has a strong impact on the fractured silicon particle distribution under monotonic (Gurland and Plateau, 1963; Yeh and Liu, 1996; Dighe and Gokhale, 1997) and cyclic (Gall et al., 1999b) loading conditions, the model did not capture the geometrical aspects of particle fracture. Localized plastic flow near the particles will lead to dislocation pileups and hardening at the microscale. However, it is insufficient to exclusively consider the local pileup stresses as influenced by the external loading, regardless of the particle geometry. The driving force for particle fracture is also affected by the distribution of mismatch stresses (stresses due to a difference in mechanical flow properties between the particle and matrix). If the mismatch stresses did not influence particle fracture, particles would be expected to fracture in a random distribution, irrespective of the particle geometry. However, particles with high aspect ratios consistently show an increased propensity for fracture (Gurland and Plateau, 1963; Yeh and Liu, 1996; Dighe and Gokhale, 1997). In addition, the fracture plane in the silicon is usually perpendicular to the applied loading axis (Gurland and Plateau, 1963; Yeh and Liu, 1996; Dighe and Gokhale, 1997). These two effects are arguably the most dominant ones observed in micrographs, and they are both predicted by continuum analysis of the particles (Gurland and Plateau, 1963). Consequently, the fracture and debonding of silicon particles in a ductile aluminum matrix can be properly modeled by calculating stress values near the particles using a continuum-based approach. An accurate continuum analysis must capture stresses due to mismatches of the elastic and plastic flow properties between the two phases. Other effects such as the relative cleavage plane and slip system orientation will also play a role in the particle fracture (Yeh and Liu, 1996). However, due to the low anisotropy of aluminum coupled with the multiple cleavage plane variants in silicon, it is probable that the geometrical features of particles overshadow these effects.

The current lack of agreement over the relative importance of different mechanisms for local silicon particle fracture is partially due to the complexity of extracting quantitative information from metallurgical studies. Quantifying the relative importance of different microscopic parameters on particle fracture and debonding will facilitate the development of improved monotonic and cyclic micromechanical models. Such models should include more than just the volume fraction of second phase inclusions as a microstructural parameter.

The present study will provide further insight into the parameters influencing silicon particle fracture and debonding in an aluminum matrix using a continuum analysis. The study is unique because it considers cyclic boundary conditions (tensile-compressive) and Al–Si microstructures representative of actual distribution and morphological parameters in cast Al–Si alloys. To accurately represent particle geometry, particle interactions, and the stress–strain behavior of the aluminum matrix, the finite element method is employed. The silicon particles are modeled using an isotropic linear elastic stress–strain relationship. The aluminum matrix material is modeled using an internal state variable plasticity model (Bammann et al., 1993, 1996). The plasticity model incorporates yield criterion and flow rules motivated from dislocation mechanics and thus captures the overall effects of lower length scale phenomenon such as dislocation pileups, dislocation generation, and anisotropic hardening. The material constants for the model are determined from experimental cyclic stress–strain curves for the aluminum matrix material (Al–1%Si) in A356 cast Al. The use of such a model also allows the application of far-field cyclic boundary conditions since history effects are inherent to the model. Further details on the constitutive model and finite element meshes are covered in the following section.

The numerical investigation will consider parameters known to affect particle fracture and debonding based on previous metallurgical studies, such as particle shape, relative particle size, and particle alignment (Gurland and Plateau, 1963; Yeh and Liu, 1996; Dighe and Gokhale, 1997; Gall et al., 1999a). In addition, some parameters, which are difficult to rationalize from metallurgical observations, will be studied to quantify their relative influence on the fracture and debonding of silicon particles. The latter parameters include particle spacing, particle configuration, grouping of particle clusters, and microporosity. The advantage of using idealized microstructures to study particle fracture and debonding is that the quantitative influence of all parameters can be studied independently. In metallurgical studies, it is difficult to independently quantify the effects of microstructural parameters when complex interactions are inherent. The quantitative predictions of the numerical study are presented in light of metallurgical findings to assure that the numerical results provide insights that are consistent with observations. In addition, the numerical study will compare the effects of particle debonding versus particle fracture. Particle debonding has received considerably less attention than particle fracture even though it is important during the initial stages of fatigue crack growth in Al–Si alloys (Gall et al., 1999b). Our numerical study does not explicitly consider the mechanics of debonding since this issue has been previously addressed (Needleman, 1987). In addition, particle fracture is assumed to occur instantaneously at a critical stress level due to the brittle nature of silicon particles. We focus on the effect of fully bonded, partially debonded, and fractured silicon particles on the subsequent initiation of debonding and fracture in neighboring particles. A design of experiment (DOE) methodology (Devor et al., 1992) is utilized to help reduce the number of finite element models necessary to systematically determine the effects of all seven parameters in all three damaged states. Ultimately, 48 unique finite element meshes and analyses are required to obtain the desired information. Although the numerical analyses pertain to the behavior of a cast A356 aluminum alloy, the results provide insight into the debonding and fracture characteristics for any alloy system with stiff and strong particles which are surrounded by a work hardenable matrix.

2. Finite element modeling

2.1. Material models

Cast Al–Si alloys contain a mixture of a eutectic phase (Si particles embedded in an Al–1% Si matrix) and a proeutectic Al–1%Si phase. Depending on the alloy type, trace amounts of other elements are also present to promote precipitation hardening or improve other casting properties. The focus of this finite element study is on the silicon particles (the inclusions) embedded in the Al–1%Si phase (the matrix). The silicon particles are assumed to behave in an isotropic linear elastic manner with an elastic modulus of $E_s = 130$ GPa and a Poisson's ratio of 0.28. The aluminum matrix material is described using an internal state variable plasticity model with coupled microvoid growth (Bammann et al., 1993, 1996). The model captures the dependence of plastic flow on strain rate, temperature, and large strain deformation. However, in the present paper, the temperature and strain rate dependence of the model were not utilized to keep the study succinct. A thorough analysis of the relevant equations, assumptions, and predictive capability of the model is found in a previous publication (Bammann et al., 1993). However, for the sake of completeness, the important equations are summarized below. *All constants for the model* were determined by fitting (non-uniquely) the predicted stress–strain response to the uniaxial experimental data using a least squares data fit. The experimental and model stress–strain curves for the Al–1%Si matrix material are shown in Fig. 1 for cycles 1, 2, and 10. In both the model and the experiment, the evolution of the stress–strain response saturates after 10 cycles.

The constitutive model for the aluminum matrix assumes an additive decomposition of the deformation rate, \underline{D} , and the spin tensor, \underline{W} :

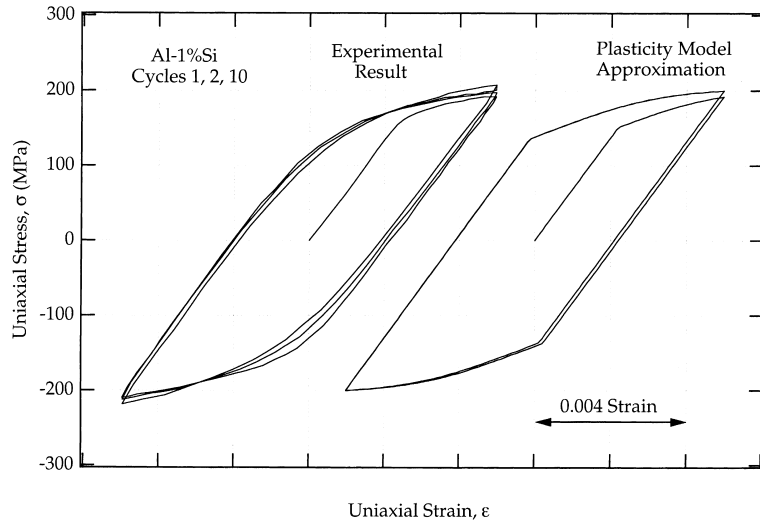


Fig. 1. Experimental and model stress–strain response for the Al–1%Si matrix material in the finite element simulations.

$$\underline{D} = \underline{D}^e + \underline{D}^p + \underline{D}^v, \tag{1}$$

$$\underline{W} = \underline{W}^e + \underline{W}^p, \tag{2}$$

where the superscripts e, p, and v denote elastic, deviatoric plastic, and volumetric components respectively. These large strain deformation tensors are defined in traditional continuum mechanics textbooks. A letter with an underscore represents a second-order tensor, while a letter without an underscore is a scalar. The elastic deformation tensor, \underline{D}^e , is embedded in a linear quasi-elastic relationship given by

$$\dot{\underline{\sigma}} = (1 - \phi) \left[\left(k - \frac{2}{3} G \right) \text{tr}(\underline{D}^e) \underline{I} + 2G \underline{D}^e \right] - \frac{\dot{\phi}}{(1 - \phi)} \underline{\sigma}, \tag{3}$$

where $\underline{\sigma}$ and $\dot{\underline{\sigma}}$ are the Cauchy stress and the co-rotational rate of the Cauchy stress respectively, ϕ is an internal state variable that represents the void volume fraction, and $k = 67.6$ GPa and $G = 25.9$ GPa are the room temperature elastic bulk and shear moduli, respectively, and \underline{I} is the second-order identity tensor. The plastic deformation tensor, \underline{D}^p , is given by the following relationship:

$$\underline{D}^p = f \sinh \left[\frac{|\underline{\sigma}' - (2/3)\underline{\alpha}'| - (\kappa + Y)(1 - \phi)}{(1 - \phi)} \right] \frac{\underline{\sigma}' - (2/3)\underline{\alpha}'}{\|\underline{\sigma}' - (2/3)\underline{\alpha}'\|}, \tag{4}$$

where $Y = 147.5$ Mpa is the initial yield strength of the material at room temperature, $f = 1 \times 10^{-5}$ is a constant, and $\underline{\sigma}'$ is the deviatoric Cauchy stress. The terms κ and $\underline{\alpha}'$ are internal state variables representing isotropic hardening and deviatoric kinematic hardening, respectively. The double bars in Eq. (4) represent the norm of enclosed tensors. The volumetric deformation tensor, \underline{D}^v , is given by the following relationship:

$$\underline{D}^v = \frac{1}{3} \text{tr}(\underline{D}) \underline{I}. \tag{5}$$

The evolution equations for the three internal state variables ϕ , κ , and $\underline{\alpha}$ are given as follows:

$$\dot{\underline{\alpha}} = h\underline{D}^p - r\frac{2}{3}\underline{D}^p\|\underline{\alpha}\|\underline{\alpha}, \quad (6)$$

$$\dot{\kappa} = H\|\underline{D}^p\| - R\frac{2}{3}\|\underline{D}^p\|\kappa^2, \quad (7)$$

$$\dot{\phi} = \sqrt{\frac{2}{3}}\sinh\left[\frac{2(2n-1)}{3(2n+1)}\frac{I_1}{\sqrt{3J_2}}\right]\left[\frac{1}{(1-\phi)^n} - (1-\phi)\right]\|\underline{D}^p\|, \quad (8)$$

where the constants $h = 2503$ MPa and $H = 1000$ MPa are hardening terms and $r = 8.45$ MPa and $R = 2.00$ MPa are dynamic recovery terms for the Al–1%Si matrix material. The evolution equation for microporosity is dictated exclusively by a Cocks–Ashby void growth rule (Cocks and Ashby, 1980). Microporosity much smaller than the silicon particles is possible due to the rejection of hydrogen gas at the liquid–solid interface during solidification, but it is difficult to quantitatively measure. The micropores exist at a much smaller length scale than shrinkage assisted gas porosity traditionally viewed in metallurgical studies. The constant $n = 0.3$ is a void growth parameter determined from notched tensile tests on cast Al–Si alloys. The damage parameter ϕ is initialized at 0.00 or 1×10^{-7} depending on the initial volume fraction of porosity for a particular finite element run. The stress invariants in Eq. (8) are given as:

$$I_1 = \sigma_1 + \sigma_2 + \sigma_3, \quad (9)$$

$$J_2 = \frac{1}{6}\left[(\sigma_1 - \sigma_2)^2 + (\sigma_2 - \sigma_3)^2 + (\sigma_3 - \sigma_1)^2\right], \quad (10)$$

where σ_1 , σ_2 , and σ_3 are principal stresses.

2.2. Morphological parameters and meshes

The seven parameters to be considered in this study are summarized in Fig. 2. The ranges of the parameters in Fig. 2 were determined by examining multiple micrographs provided from a previous study on a cast A356 aluminum alloy with modified silicon particles (Dighe and Gokhale, 1997). Unmodified alloys were not considered since they are of little interest from a practical standpoint due to insufficient mechanical properties, such as low tensile ductility. We recognize that more extreme values than indicated in Fig. 2 could exist in the microstructure for all of the different parameters. However, the high and low values in Fig. 2 represent a statistically significant deviation from the norm for a given parameter. The proposed ranges are sufficient to screen the relative influence of the parameters on the debonding and fracture characteristics of the silicon particles. Once these first-order effects are understood, the more dominant parameters can be studied over a wider range of values in future studies. With exception to microporosity, all of the parameters in Fig. 2 are visually quantifiable in typical micrographs.

To systematically study the effect of the seven parameters on particle fracture and debonding, a two-level factorial DOE methodology was incorporated (DeVor et al., 1992). Such a DOE study provides both main effects and interaction effects. A main effect, E , is a quantitative measurement of the average shift in the measured system response due to a change in an input parameter value from the low to high setting. For example, the quantitative main effect of the particle shape parameter on the largest principal stress in the silicon particle, σ_1 , is the difference in σ_1 for an elliptical versus a round particle. An interaction effect quantifies how the magnitude of the main effect for a given parameter depends on the other parameters in the DOE study. In this study, only main effects are reported since interaction effects were either negligible or

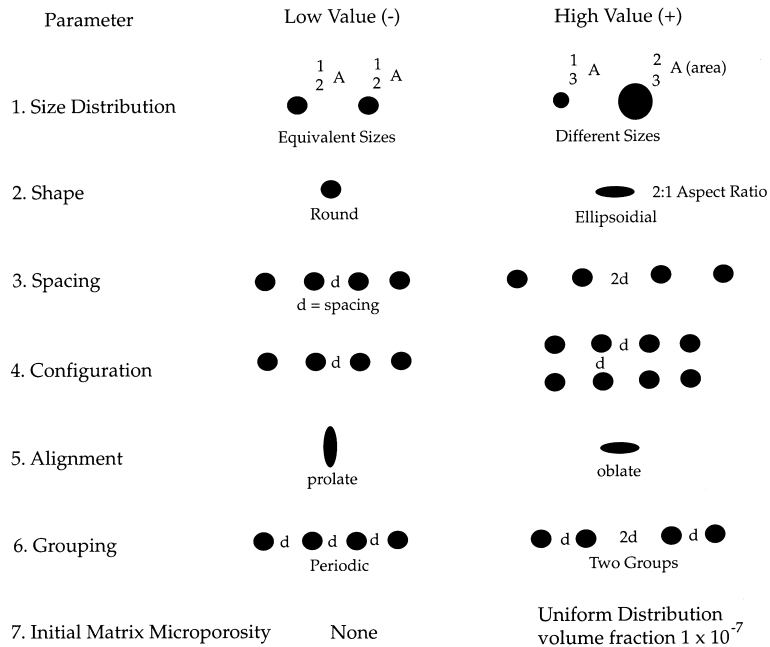


Fig. 2. Schematic demonstrating the different parameters considered in the present finite element study. The parameter ranges were determined by examining actual micrographs of a modified cast A356 aluminum alloy.

obvious from a physical standpoint. For example, a large interaction between particle shape and alignment was uncovered. An interaction between shape and alignment is consistent with expectations since round particles demonstrate no alignment effects, however, elliptical particles demonstrate significant alignment effects. Table 1 demonstrates the test matrix for studying the effects of silicon particle morphology on particle debonding and fracture in cast Al–Si alloys, for each of the three cases of intact, fractured, and debonded particles. The high (+) and low (–) levels for the silicon morphological parameters are elucidated in Fig. 2.

For each of the 16 configurations dictated by Table 1, a representative finite element mesh was constructed. In the interest of space limitations, it is impractical to show all of the finite element meshes; however, a schematic of run number 10 is shown in Fig. 3(a). The silicon particles are enlarged for clarity, and their actual size is indicated in the lower left corner of Fig. 3(a). In run 10 all of the parameters have the high (+) values (Table 1). The finite element analyses were conducted using the code ABAQUS (1994) which employs a user material subroutine containing the aforementioned plasticity model. The finite element models were two-dimensional plane strain analyses with four noded isoparametric elements. The overall mesh size was $240 \times 240 \mu\text{m}$ to alleviate any boundary edge effects. Furthermore, because the boundaries remained orthogonal, periodicity is essentially included. The spacing parameter d in Fig. 3 was always $4 \mu\text{m}$. In all meshes the total area fraction of silicon particles was also kept arbitrarily constant at 0.174%, regardless of the shape and number of silicon particles. The low value of 0.174% is chosen to alleviate any edge (surface) interactions on silicon particle fracture and debonding. Each mesh contained approximately 10 000 elements and the fine mesh near the particles contained elements on the order of 0.1 times the particle size. Fig. 3(b) is a typical example showing the fine mesh region near the silicon particles for mesh number 10. The applied far-field boundary condition was a cyclic tension–compression strain (displacement) with an amplitude of 0.4% for three cycles. The original 16 meshes contained silicon particles that were all perfectly bonded to the Al–1%Si matrix. Each mesh was then modified to contain two

Table 1

The design matrix used to create different finite element meshes to study of the effect of morphological parameters on the debonding and fracture of silicon particles embedded in an Al–1%Si matrix. A prolate particle has a major axis parallel to the loading axis, while an oblate particle has a major axis perpendicular to the loading axis

Mesh #	Size distribution	Particle shape	Particle spacing	Configuration	Particle alignment	Grouping effect	Microporosity
1	Uniform (-)	Round (-)	d (-)	4 (-)	Prolate (-)	No (-)	No (-)
2	Non-uniform (+)	Round (-)	d (-)	4 (-)	Oblate (+)	Yes (+)	No (-)
3	Uniform (-)	Ellipse (+)	d (-)	4 (-)	Oblate (+)	No (-)	Yes (+)
4	Non-uniform (+)	Ellipse (+)	d (-)	4 (-)	Prolate (-)	Yes (+)	Yes (+)
5	Uniform (-)	Round (-)	$2d$ (+)	4 (-)	Oblate (+)	Yes (+)	Yes (+)
6	Non-uniform (+)	Round (-)	$2d$ (+)	4 (-)	Prolate (-)	No (-)	Yes (+)
7	Uniform (-)	Ellipse (+)	$2d$ (+)	4 (-)	Prolate (-)	Yes (+)	No (-)
8	Non-uniform (+)	Ellipse (+)	$2d$ (+)	4 (-)	Oblate (+)	No (-)	No (-)
9	Uniform (-)	Round (-)	d (-)	8 (+)	Prolate (-)	Yes (+)	Yes (+)
10	Non-uniform (+)	Round (-)	d (-)	8 (+)	Oblate (+)	No (-)	Yes (+)
11	Uniform (-)	Ellipse (+)	d (-)	8 (+)	Oblate (+)	Yes (+)	No (-)
12	Non-uniform (+)	Ellipse (+)	d (-)	8 (+)	Prolate (-)	No (-)	No (-)
13	Uniform (-)	Round (-)	$2d$ (+)	8 (+)	Oblate (+)	No (-)	No (-)
14	Non-uniform (+)	Round (-)	$2d$ (+)	8 (+)	Prolate (-)	Yes (+)	No (-)
15	Uniform (-)	Ellipse (+)	$2d$ (+)	8 (+)	Prolate (-)	No (-)	Yes (+)
16	Non-uniform (+)	Ellipse (+)	$2d$ (+)	8 (+)	Oblate (+)	Yes (+)	Yes (+)

fractured or two debonded silicon particles within the cluster of silicon particles, resulting in 32 additional finite element meshes. The two damaged particles were always the same as indicated on Fig. 3 for clusters of silicon particles. The fractured particles were modeled by introducing a crack across the center of the particles perpendicular to the applied loading axis. The debonded particles had a crack introduced along the interface between the silicon particle and the Al–1%Si interface, only on the lower half of the particle. Crack face boundary conditions were considered by treating the exposed elements as frictionless surface contact elements. The contact conditions prevented the crack faces from passing one another during local compressive stress states. For the cases of cracked or debonded particles, the defects were introduced at the onset of the deformation.

Two different stress values were extracted from each of the 48 finite element analyses during the third loading cycle at the point of maximum applied tensile stress: (1) The maximum tensile principal stress in a silicon particle, and (2) the maximum tensile hydrostatic stress at the interface between a silicon particle and the Al–1%Si matrix material. The hydrostatic stress was created by contributions from all three principal directions in this plane strain analysis. The principal stress in the particle is a proposed measure of the driving force for silicon particle fracture. Likewise, the hydrostatic stress at the particle–matrix interface is a measure of the driving force for silicon particle debonding (Needleman, 1987). In the meshes where the particles were debonded or cracked a priori, the pre-damaged particles were not considered in the determination of stress values. In these cases, the aim was to quantify how the debonding and fracture of adjacent particles affected the stress distribution in neighboring, intact particles. We note that the third cycle was chosen to allow some cyclic hardening to occur. In the present constitutive model the stress–strain response saturates near the third cycle. In any case, there may be some differences in the response between the first and the tenth cycles, for example, but the differences are small compared to the large differences for the different meshes, which are the focus of the present study. The applied strain amplitude was kept relatively low since we are concerned with the implications of the study on high cycle fatigue of cast Al–Si alloys. We also note that the residual stresses created during the cool-down of the material are often a factor related to the deformation of metal matrix composites. We could not find literature demonstrating that residual stresses were a factor for cast Al–Si alloys, thus we did not consider them here.

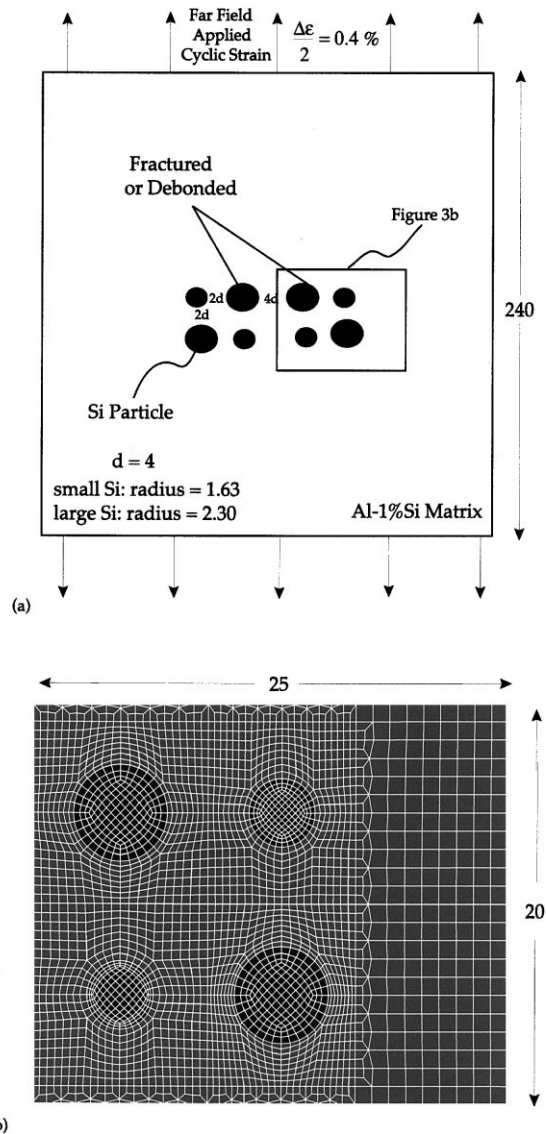


Fig. 3. (a) Schematic of mesh 10 with the silicon particles enlarged to highlight their distribution. The actual radii are given in mesh units on the lower left corner of the mesh. (b) The finite element fine mesh region near the silicon particles in mesh 10.

3. Screening of dominant parameters

The data from the finite element analyses are presented in Table 2. Each data point represents a maximum stress value (hydrostatic or principal) from an individual finite element analysis. The data in the columns labeled "Bond" were extracted from analyses where the silicon particles were all perfectly bonded within the given mesh. The data in the "Crack" and "Debond" columns were extracted from analyses where two silicon particles in the cluster were cracked or debonded respectively (Fig. 3). It is difficult to visualize the relative importance of the seven parameters by inspection of the data in Table 2. However, by

Table 2

Results from the 48 finite element analyses on the 16 meshes in Table 1. All values were taken from bonded silicon particles during the point of maximum tensile stress in the third loading cycle. Bond, Crack, and Debond differentiate between meshes with all perfectly bonded particles, two cracked particles, and two debonded particles respectively

Mesh #	Maximum principal stress within a fully bonded silicon particle σ_1 (MPa)			Maximum hydrostatic stress at the Si–Al interface of a bonded Si particle, σ_H (MPa)		
	Bond	Crack	Debond	Bond	Crack	Debond
1	267	281	325	153	160	185
2	267	288	339	156	160	185
3	252	288	339	139	160	185
4	308	302	380	175	171	185
5	267	267	284	153	153	160
6	267	274	291	153	153	175
7	302	302	312	175	171	175
8	248	274	289	139	153	175
9	267	281	300	153	164	175
10	267	281	312	153	164	195
11	252	274	298	139	167	190
12	302	302	328	175	175	195
13	267	267	279	153	153	165
14	267	267	279	153	153	165
15	302	302	311	175	171	170
16	248	269	273	139	153	165

performing the appropriate DOE transformation on the six data columns in Table 2, the data reveal the quantitative effects of the seven parameters. The meaning of the DOE data transformation is covered in detail in DeVor et al. (1992); however, an overview of the required calculations is presented in Appendix A.

From the data in Table 2, the main effects of the silicon particle parameters on silicon particle fracture and debonding are presented in Figs. 4–6. In the cases where all of the particles are perfectly bonded, shape and alignment are by far the most dominant effects on particle fracture (Fig. 4(a)) and particle debonding (Fig. 4(b)). Within the range considered here, the five remaining parameters are shown to have a negligible effect on the initiation of fracture or debonding of silicon particles in an Al–1%Si matrix. Once several of the particles within a group are cracked, the effect of particle spacing enters as a significant effect as demonstrated in Fig. 5(a) and (b). When several silicon particles within the groupings are partially debonded (Fig. 6(a) and (b)), the effect of particle spacing becomes more dominant than the other parameters studied.

4. Discussion

Depending on the damaged state of neighboring particles, the finite element results indicate that the following parameters, listed in descending order of importance, have a significant influence on the debonding and fracture of silicon particles in a Al–1%Si matrix:

1. particle shape;
2. particle alignment;
3. particle spacing;
4. particle configuration.

To elucidate the influence of the four dominant parameters on fracture and debonding of silicon particles it is necessary to examine the stress distributions in the silicon particles and in the surrounding Al–

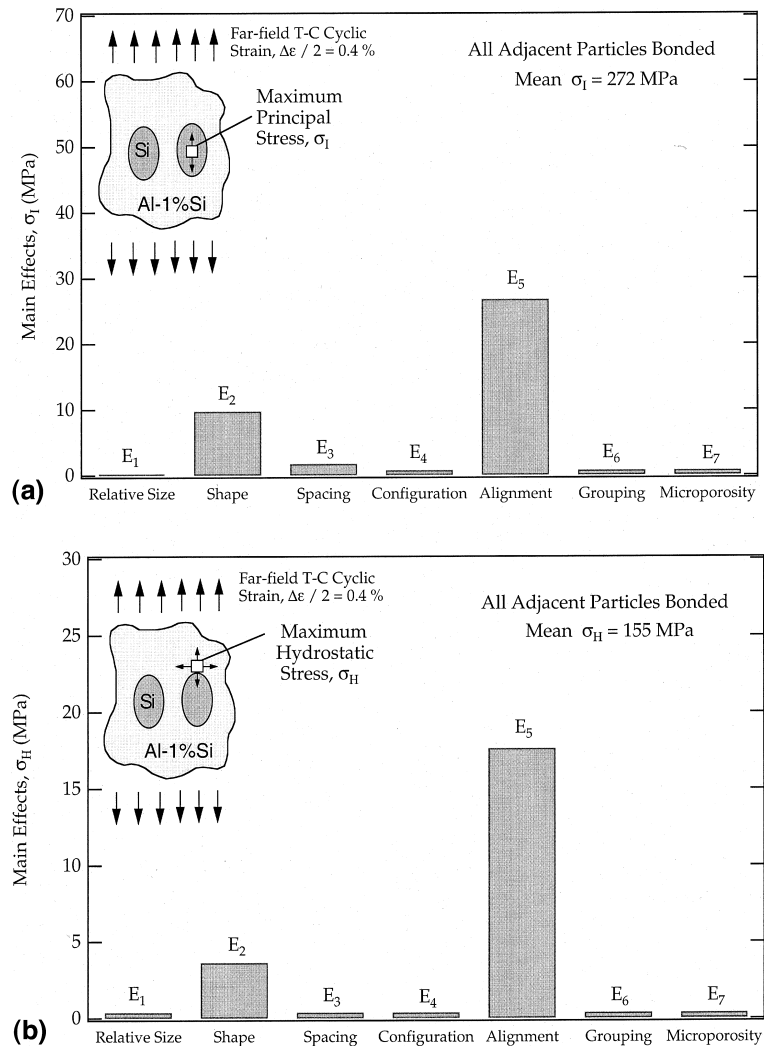


Fig. 4. The quantitative main parameter effects on (a) particle cracking and (b) particle debonding. All of the adjacent particles are bonded.

1%Si matrix. The representative meshes used to study the dominant effects are numbers 10, 11, and 12 (Table 1). Figs. 7–9 show contour plots of the maximum principal tensile stresses near the silicon particles. Figs. 10–12 are contour plots of the hydrostatic stresses near the silicon particles (tensile hydrostatic stresses are negative). The contour plots in Figs. 7–12 are symmetric about the left border, such that each analysis contains eight particles. The far-field loading axis is vertical in the plane of the figures. Furthermore, Figs. 7–12 all contain three different damaged particle states: (a) all particles intact, (b) two particles cracked, (c) two particles debonded. In the fractured particles, the center crack runs through the entire silicon particle. The debonded particles have cracks that cover the lower half of the particles along the interface between the silicon and Al-1%Si materials. The contour plots were all created at the maximum applied tensile stress on the third loading cycle. Given this information, we will now discuss the effects of individual parameters on silicon particle fracture and debonding.

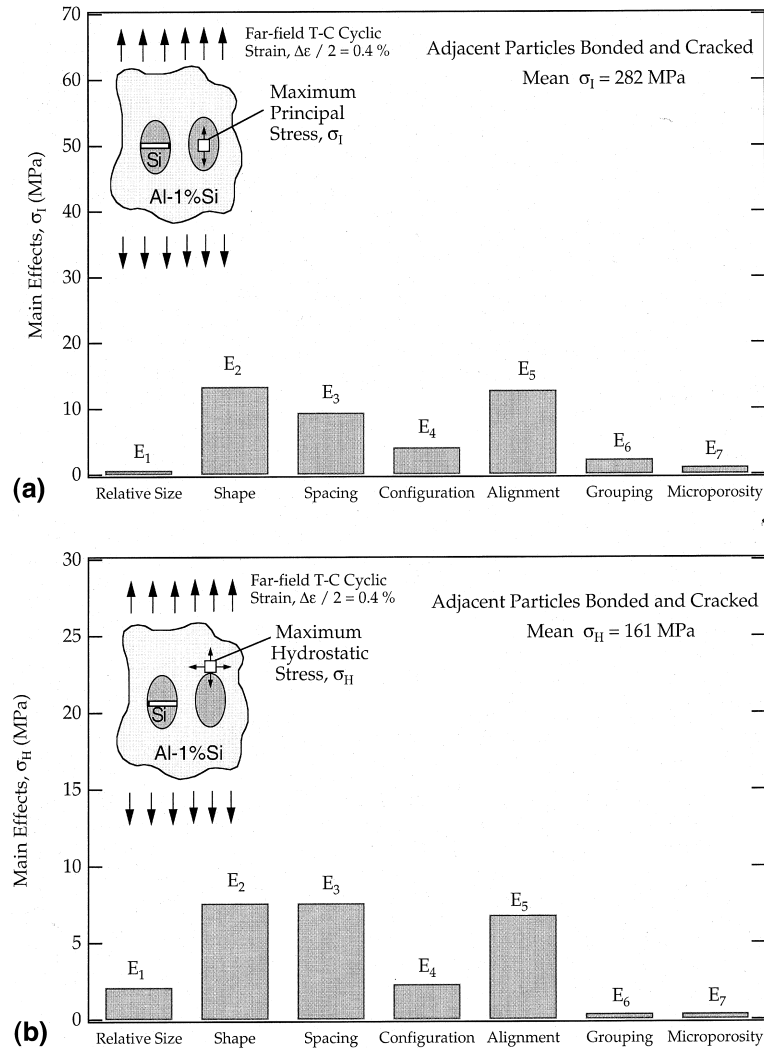


Fig. 5. The quantitative main parameter effects on (a) particle cracking and (b) particle debonding. Some of the adjacent particles are bonded while others are cracked.

4.1. Particle shape and alignment

The influences of particle shape and alignment on particle fracture for monotonic and cyclic loading are the most heavily documented effects in the materials science literature (Gurland and Plateau, 1963; Yeh and Liu, 1996; Dighe and Gokhale, 1997; Gall et al., 1999b). The influence of shape and alignment on the debonding of silicon particles has received significantly less attention (Dighe and Gokhale, 1997; Gall et al., 1999b). Previously, particle shape and alignment effects have been experimentally observed without considering a systematic variation in other relevant microstructural features. The present study demonstrates the influence of particle shape and alignment relative to other pertinent microstructural parameters such as spacing. The numerical results presented here confirm earlier predictions for isolated intact particles (Gurland and Plateau, 1963), and extend these understandings to the cases where adjacent particles are

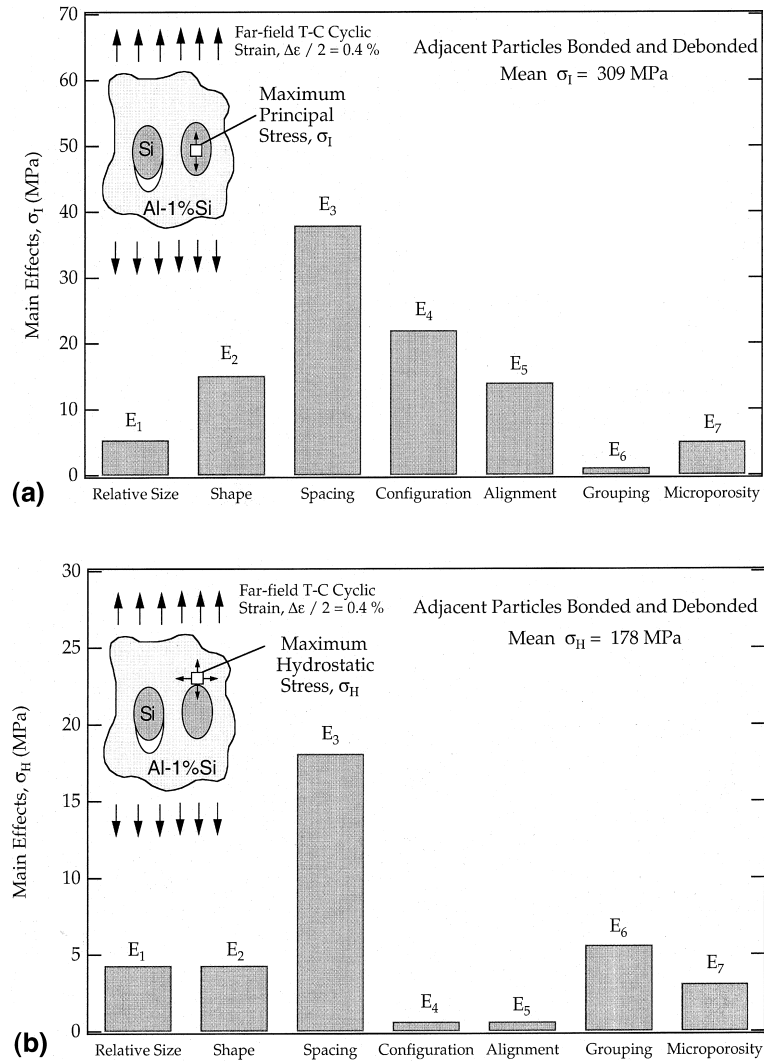


Fig. 6. The quantitative main parameter effects on (a) particle cracking and (b) particle debonding. Some of the adjacent particles are bonded while others are debonded.

fractured or debonded. When all of the particles within a cluster are intact, the maximum tensile stress in the particles and the maximum hydrostatic stress at the particle–matrix interface are greatest when the major axis of the particle is parallel to the far-field loading direction (Figs. 9(a) and 12(a)). When the particles are rounded (Figs. 7(a) and 10(a)), the stress levels inside and surrounding the particles are smaller than the stresses near particles with an elongated axis parallel to the loading direction. Furthermore, when the major axis of a particle is perpendicular to the applied loading axis (Figs. 8(a) and 11(a)), the stress levels in and around the particles are even lower than the stresses near the rounded particles.

The principal stresses within the particles are relatively uniform, regardless of the orientation of the elliptical particle. The hydrostatic stress at the particle–matrix interface is always a maximum at the top and bottom of a particle along a line parallel to the uniaxial loading axis and through the center of the particle.

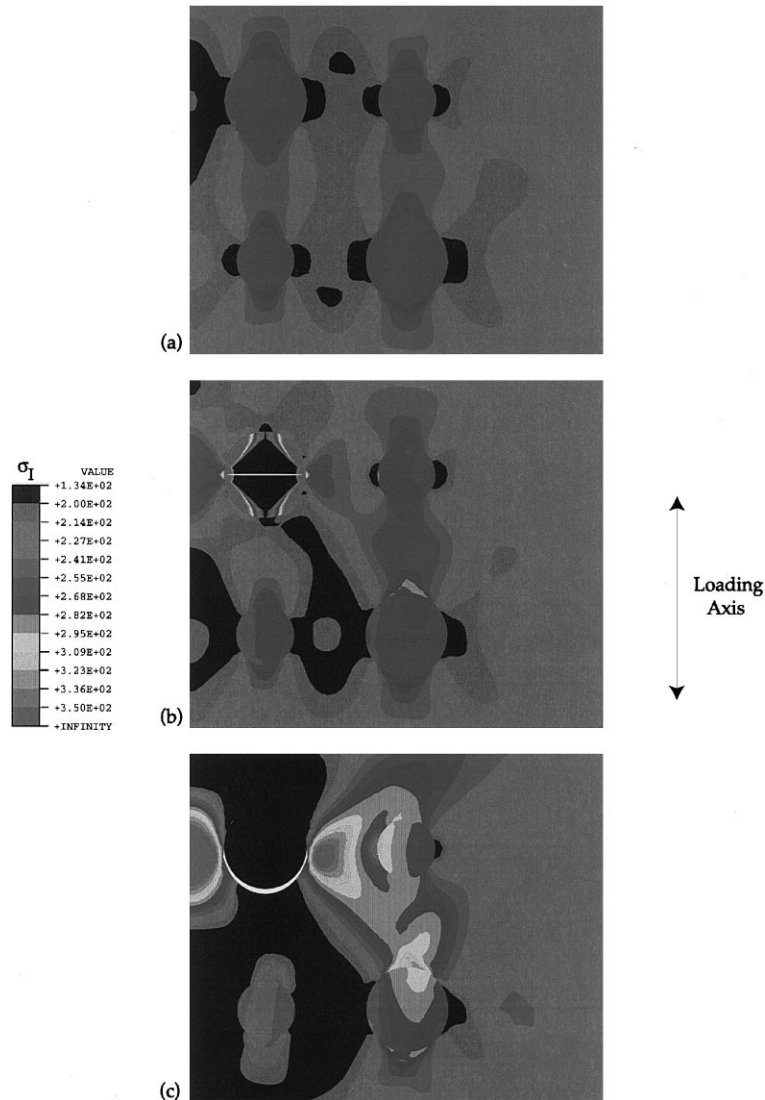


Fig. 7. Contours of the maximum principal stress, σ_1 (MPa), surrounding the silicon particles for mesh 10 at the maximum applied tensile stress in the third loading cycle. The results are symmetric about the left boundary of the plot. The mesh has three different initial configurations: (a) all particle bonded, (b) two particles cracked and (c) two particles debonded.

As the local particle radius of curvature is decreased at the top or bottom of the particle, the maximum local hydrostatic stress at the particle–matrix interface increases. For example, a particle with a major axis parallel to the loading axis (Fig. 12(a)) has an extremely small radius of curvature at the top of a particle compared to a particle with the major axis perpendicular to the loading axis (Fig. 10(a)). Consequently, the maximum hydrostatic stress at the particle–matrix interface is much greater in elongated particles aligned parallel to the loading axis (Fig. 12(a)) versus round particles (Fig. 10(a)) or elongated particles aligned perpendicular to the loading axis.

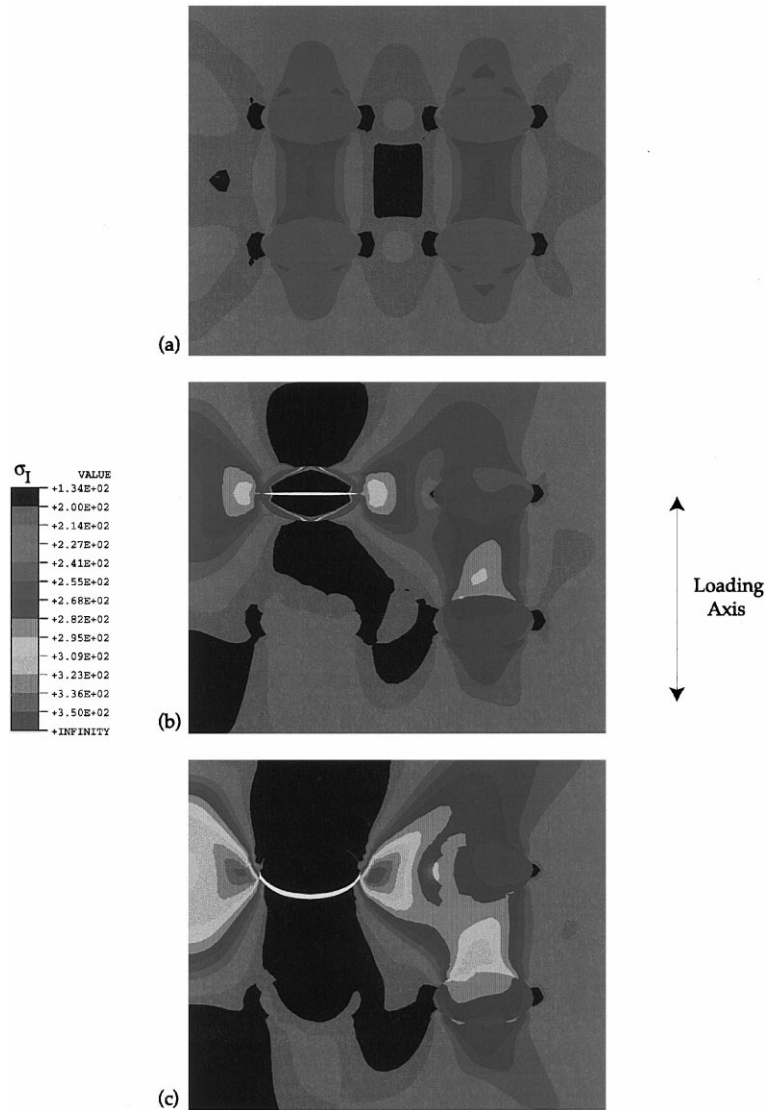


Fig. 8. Contours of the maximum principal stress, σ_1 (MPa), surrounding the silicon particles for mesh 11 at the maximum applied tensile stress in the third loading cycle. The results are symmetric about the left boundary of the plot. The mesh has three different initial configurations: (a) all particle bonded, (b) two particles cracked and (c) two particles debonded.

When several particles in a cluster are fractured across their center, the effects of particle shape and alignment are still the dominant influences on particle fracture and debonding of surrounding particles. Irrespective of the shape or alignment of the pre-cracked particle, the intensification of local stresses occurs primarily within the cracked particle (Figs. 7(b)–12(b)). The Al–1%Si matrix surrounding fractured particles experiences a stress localization over a length scale depending on the shape and alignment of the particle. Although intact particles with a major axis perpendicular to the applied loading axis possess a higher resistance to particle fracture, fractured particles with such orientations facilitate the highest local principal and hydrostatic stresses in the surrounding Al–1%Si matrix. For example, in Fig. 8(b), a zone of

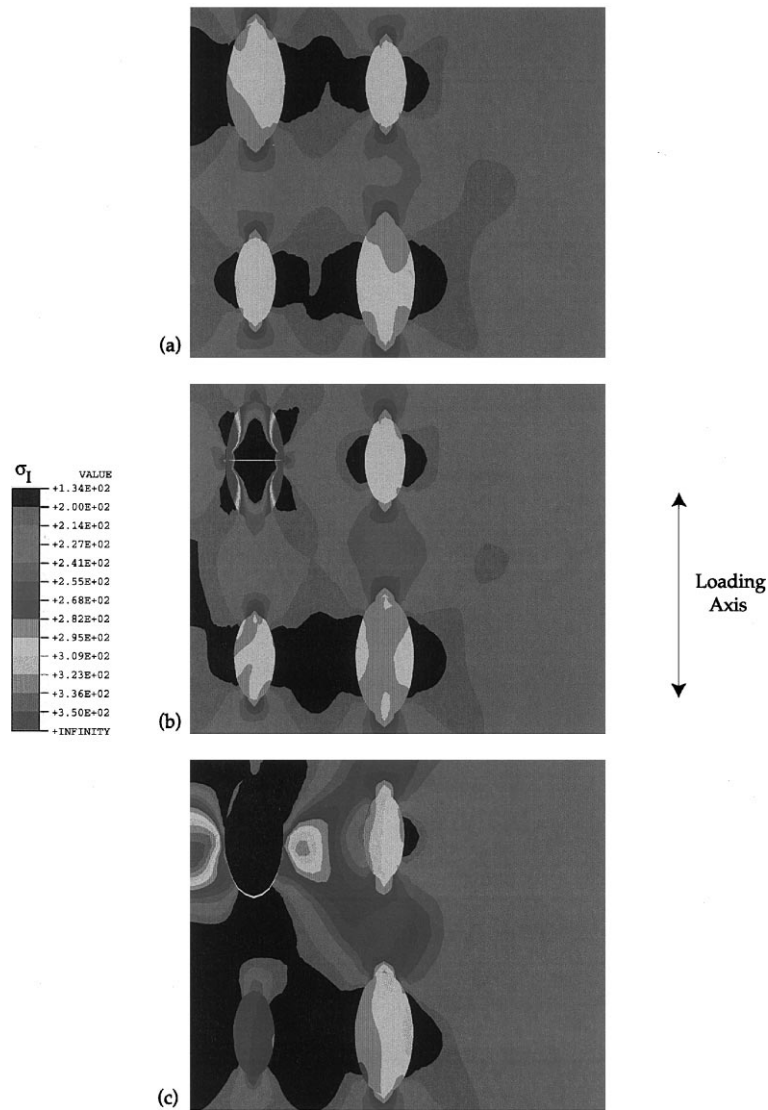


Fig. 9. Contours of the maximum principal stress, σ_1 (MPa), surrounding the silicon particles for mesh 12 at the maximum applied tensile stress in the third loading cycle. The results are symmetric about the left boundary of the plot. The mesh has three different initial configurations: (a) all particle bonded, (b) two particles cracked and (c) two particles debonded.

magnified local stresses is present in the Al–1%Si matrix near the fractured particle. However, in Fig. 9(b), the zone of intensified stresses near the cracked particle is significantly smaller than that of the cracked particle in Fig. 8(b). The smaller localized zone size in the case of the cracked particle with a major axis parallel to the loading axis is caused by differences in the crack length and constraint of the two particle halves. The cracked particle with a major axis parallel to the loading axis has a much smaller inherent defect size (crack length), and therefore the zone of enhanced plasticity and localized stresses near the crack tip are smaller. Furthermore, the cracked particle with a major axis parallel to the loading axis (Fig. 9(b)) experiences local stresses within the fractured particle which are higher and farther reaching compared to the

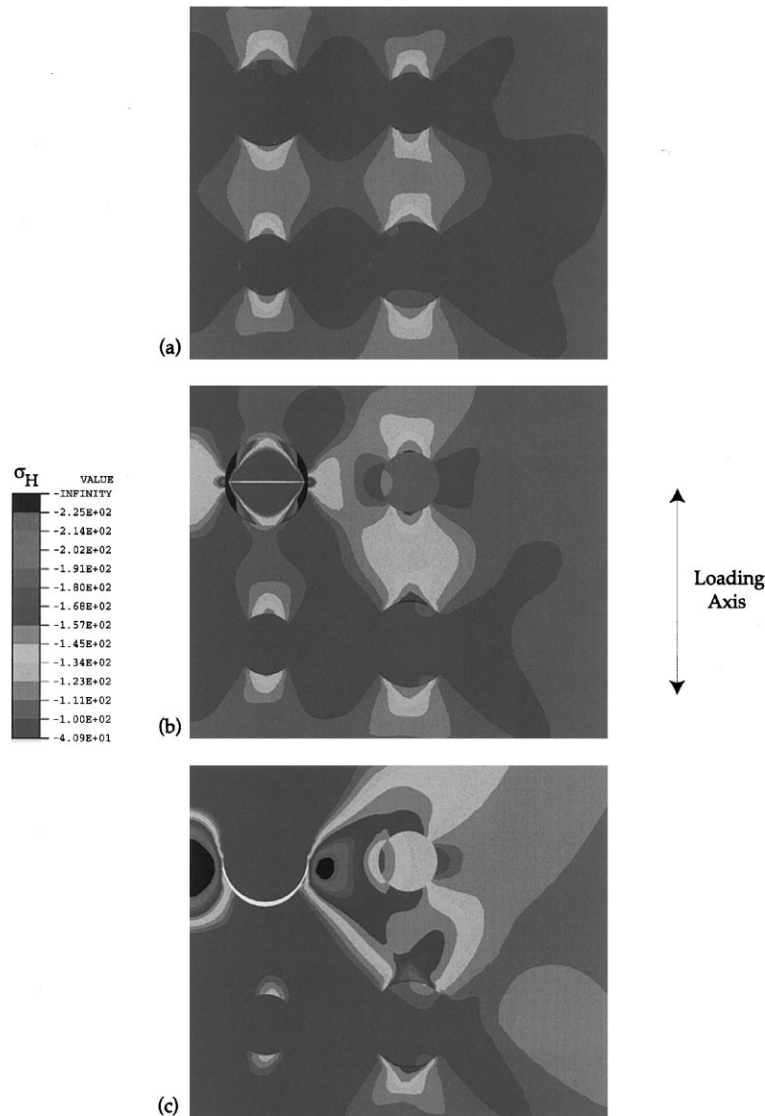


Fig. 10. Contours of the hydrostatic stress σ_H (MPa, - is tension) surrounding the silicon particles for mesh 10 at the maximum applied tensile stress in the third loading cycle. The results are symmetric about the left boundary of the plot. The mesh has three different initial configurations: (a) all particle bonded, (b) two particles cracked and (c) two particles debonded.

stresses within the particle perpendicular to the loading axis (Fig. 8(b)). Consequently, the local stresses immediately outside the fractured particle with the major axis parallel to the loading axis are smaller as expected by energetic arguments. In either orientation, the relatively small localization of stresses surrounding the fractured particles only has a negligible influence on the principal and hydrostatic stresses in neighboring intact particles (compare the stress distributions in the particles surrounding the fractured and intact particles in Figs. 7(b)–12(b) versus Figs. 7(a)–12(a)).

When several particles within a cluster debond (Figs. 7(c)–12(c)), the localization of stresses within the surrounding Al–1%Si matrix is considerably more intense compared to the intact (Figs. 7(a)–12(a)) or

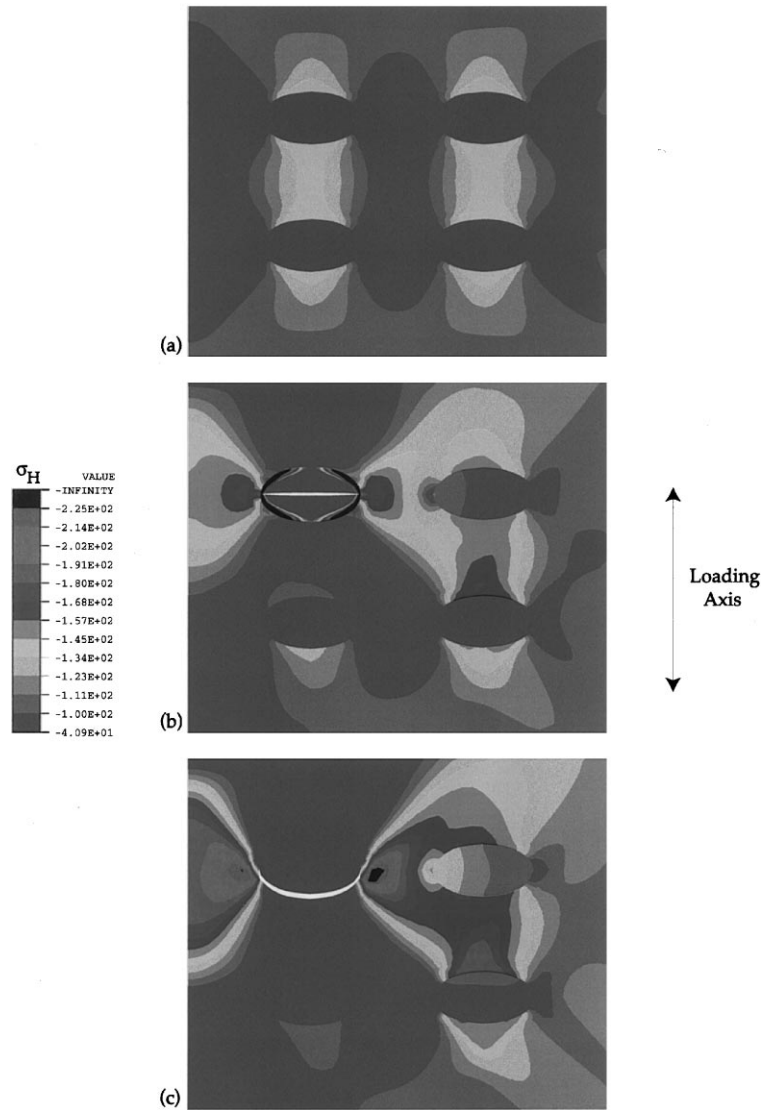


Fig. 11. Contours of the hydrostatic stress σ_H (MPa, – is tension) surrounding the silicon particles for mesh 11 at the maximum applied tensile stress in the third loading cycle. The results are symmetric about the left boundary of the plot. The mesh has three different initial configurations: (a) all particle bonded, (b) two particles cracked and (c) two particles debonded.

fractured (Figs. 7(b)–12(b)) particles. In contrast to the high stresses within fractured particles, the stresses within the debonded particles are negligible. The shape and alignment of a debonded particle has a similar influence on the localization of stresses in the Al–1%Si matrix as that of the fractured particles. If the major axis of the debonded particle is parallel to the loading axis (Figs. 9(c) and 12(c)), then the intensification of stresses is less than if the major axis of the particle is perpendicular to the loading axis (Figs. 8(c) and 11(c)). Debonded circular particles (Figs. 7(c) and 10(c)) cause stress intensification bounded by the two orientations of the elliptical particles. In the situations where adjacent particles debond, the stresses in the neighboring particles are influenced by debonded particles of all orientations and shapes. When the major

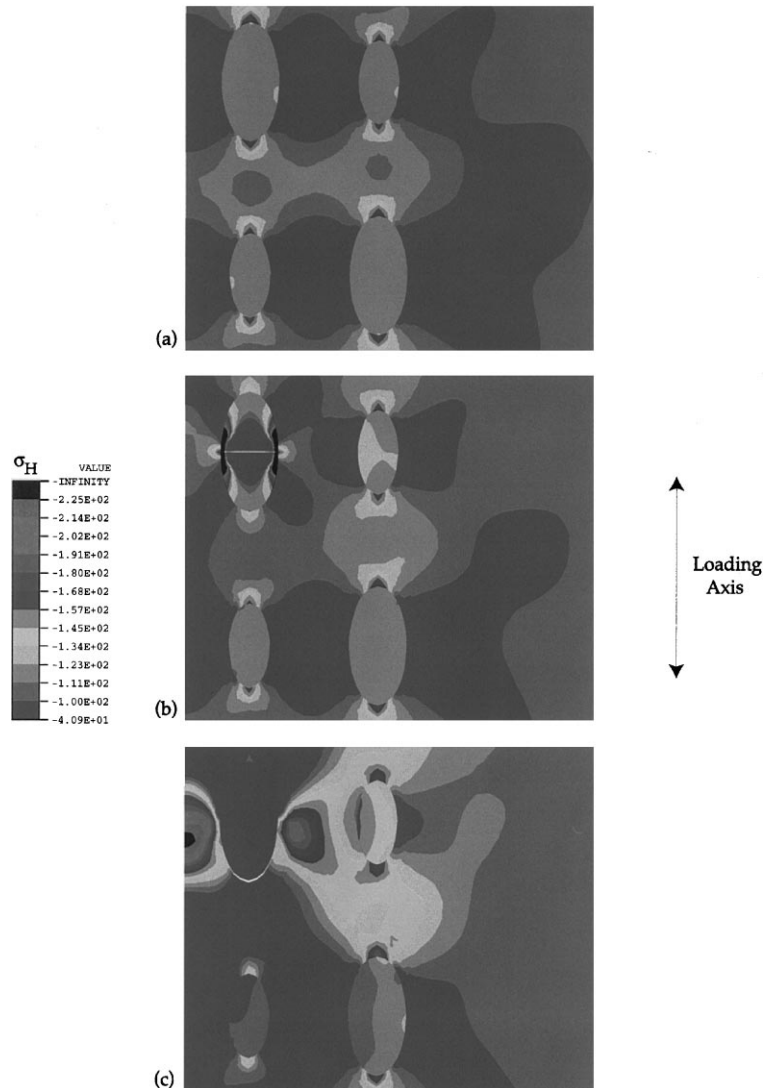


Fig. 12. Contours of the hydrostatic stress σ_H (MPa, – is tension) surrounding the silicon particles for mesh 12 at the maximum applied tensile stress in the third loading cycle. The results are symmetric about the left boundary of the plot. The mesh has three different initial configurations: (a) all particle bonded, (b) two particles cracked and (c) two particles debonded.

axis of the debonded particle is perpendicular to the loading axis the interaction with surrounding particles is the strongest.

In closing, shape and alignment are the most dominant parameters influencing particle fracture and debonding. It is extremely important to point out that in Figs. 5 and 6 shape and alignment still appear as less dominant effects compared to the other parameters. However, when particles are debonded and fractured, shape and alignment are more dominant than Figs. 5 and 6 portray due to the “average” nature of the DOE effect measures. For example, particles arranged in an array with their major axis parallel to the loading direction have the highest stress fields inside of them. However, when particles within such an array crack or debond, the crack length is small compared to fractured or debonded particles with a major axis

perpendicular to the loading axis (assuming that the cracks form perpendicular to the tensile axis). Consequently, the stress in adjacent particles due to neighbors cracking and debonding is smaller for arrays of particles parallel to the tensile axis compared to particles perpendicular to it. In other words, the particles that are most prone for cracking and debonding are also inflict the smallest increase in stresses on their neighbors after failure. The counterbalancing effects of internal (self mismatch) and external (neighbor effects) stresses for different shapes and alignments after fracture and debonding yield an anomalously low “average” effect of shape and alignment in Figs. 5 and 6.

4.2. Particle spacing

When all of the silicon particles within a cluster are intact, the local stress fields surrounding the particles are not strong enough to affect the debonding and fracture of neighboring particles. For example, in Figs. 7(a)–12(a), the stresses inside all of the particles are uniform within the bounds of numerical noise. The uniformity of stresses within an elliptical inclusion is consistent with the classical proof of Eshelby (1957) for a single isolated inclusion. Consequently, the particles do not “feel” the influence of the external stress fields from neighboring particles. In Figs. 7(a)–12(a), the particle spacing is one particle diameter. When the spacing is increased to two particle diameters, the stress distributions within the perfectly bonded particles are identical to the distributions when the particles are one diameter apart.

If several particles within a cluster are fractured, particle spacing becomes a dominant effect in addition to particle shape and alignment. The local stress intensification near a fractured particle (Figs. 7(b)–12(b)) extends over a distance significant enough to facilitate weak particle–particle interactions. Consequently, when the distance between fractured and intact particles is varied between one particle diameter and two particle diameters, the local stresses near the intact particles change. However, since the fractured particle contains much of the elastic strain energy after fracture, the spacing of neighboring particles is not as significant of an effect as in the case of debonded particles.

When several particles within a cluster debond, the spacing between particles has a strong influence on the stresses in adjacent particles. The significant increase in the stresses in particles adjacent to debonded particles (Figs. 7(c)–12(c)) is due to the larger extent of the redistributed stress fields in the Al–1%Si matrix surrounding the debonded particles. The principal stress fields within intact particles near a debonded particle show considerable gradients (Figs. 7(c)–9(c)). In addition, the debonding of adjacent particles increases the hydrostatic stresses at the particle–matrix interface of intact particles (Figs. 10(c)–12(c)). When the spacing between the particles is increased to two particle diameters, the effect of the debonded particles is weaker since the surrounding particle is not embedded in such intense local stress fields.

Essentially, the magnitude of the effect of particle spacing depends on the length scale of the stress and strain gradients outside the embedded silicon particle. If the particle spacing is on the order of the length scale where strong local stress gradients exist, then spacing will be a dominant effect. In the present study, the particle spacing was varied from one particle diameter to two particle diameters. In the intact and fractured particles, the length scale of the stress gradient was only a fraction of the particle diameter. Consequently, particle spacing does not have a strong influence on the debonding or fracture of adjacent particles when the spacing is more than a particle diameter. On the other hand, strong stress gradients near a debonded particle exist over one or two particle diameters. Therefore, the spacing between intact and debonded particles has a strong influence on the stress distributions near the intact particles when the particle spacing is varied near one or two particle diameters.

4.3. Particle configuration

When all of the silicon particles are intact, the interactions between particles are negligible. Consequently, the spatial location of adjacent particles (at a fixed distance) does not affect the stresses in particles

when all particles are intact. However, when adjacent particles are fractured or debonded, particle interactions exist. Furthermore, the spatial location of adjacent particles (at a fixed distance) has a second-order effect on the debonding and fracture of silicon particles. Figs. 8(c) and 11(c) demonstrate the effect of different particle positions on the principal and hydrostatic stress distributions in intact particles near debonded particles. Aside from a smaller absolute magnitude, configuration effects are similar for fractured particles (Figs. 8(b) and 11(b)). For all different particle orientations and shapes, intact particles at a 45° angle from a debonded particles experience the greatest principal stresses within the particle (Fig. 8(c)) and hydrostatic stress at the particle–matrix interface (Fig. 11(c)). The strong localization of stresses at a 45° angle from the debonded particle is due to “shear bands” aligned with the maximum macroscopic shear strain plane. Intact particles to the right or left (along a line perpendicular the loading axis) of debonded particles also demonstrate significant stress levels. Intact particles below or above (along a line parallel the loading axis) debonded particles demonstrate negligible stress levels.

4.4. *A note on particle size*

The results of the present study assert that relative particle size has a negligible effect on the fracture and debonding of silicon particles. However, experimental results indicate that larger particles consistently show an increased propensity for breakage and debonding (Dighe and Gokhale, 1997). There are two proposed reasons for the biased fracture of larger particles. First, the probability that a particle will contain a flaw that promotes premature fracture and debonding is greater for larger particles (Cox and Low, 1974). The effect of initial defect size within the particles was not considered in the present study, but can be superposed with the predictions made here. Second, after observing numerous micrographs of debonded and fractured silicon particles, it was concluded that the silicon particles traditionally labeled as “large” are always irregularly shaped. During solidification it is extremely difficult to form a silicon particle which is both large *and* well rounded. Consequently, based on the results of the present numerical study, it is possible that the consistent irregular shape of large silicon particles further lowers their resistance to fracture.

5. Implications on the fatigue of cast Al–Si alloys

The results of the present study have several ramifications on the understanding and modeling of the mechanical response of cast Al–Si alloys subjected to cyclic loading conditions. The results suggest that as a cast Al–Si material is cyclically loaded or exposed to overloads, the first particles crack or debond will be ones with high aspect ratios aligned with a major axis parallel to the loading axis. In addition, owing to a higher probability for internal or interface defects, larger particles of such shape and orientation will favorably fracture. Initial particle cracking and debonding is not strongly affected by neighbor interactions. Consequently, it is more important to consider the particle geometry and expected damaged state (debonded versus fractured) of individual particles rather than the local distribution during the very initial stage of fatigue (crack nucleation period).

During continued cycling, fatigue cracks will eventually form in the surrounding material at the cracked or debonded silicon particles. Based on the present results, the small growing fatigue cracks (on the order of the silicon particle size) will interact with neighboring particles and hence be affected by the distribution (configuration and spacing) of such particles. Furthermore, at such small crack sizes and crack tip driving forces, the neighboring silicon particles will act as barriers to fatigue crack propagation (Gall et al., 1999b). Consequently, isolated damaged particles are expected to produce relatively larger micro fatigue cracks during subsequent cycling. In either case, the local fatigue cracks nucleated at damaged silicon particles can have two effects on the fatigue response of the cast Al–Si alloy:

1. If no defects are present at a larger size scale, such as oxides or pores, then the distributed microcracks will grow until coalescence and final failure of the material. In this situation, the growth characteristics and rates of small microcracks within the particle-laden microstructure will have a strong influence on the fatigue life of the material. Modeling efforts of such behavior must explicitly include the effects of particle alignment, shape, spacing, and configuration on small fatigue crack growth rates.

2. If large-scale oxides and pores are present in the cast material, then a much larger dominant fatigue crack will nucleate and grow from such defects (Gall et al., 1999b). In this situation, the distributed microcracks will weaken the material ahead of the dominant fatigue crack and, on average, lower the cast materials resistance to long fatigue crack propagation. Modeling efforts of such an effect can simply incorporate a continuum damage approach, for example, that effectively elevates the Paris law crack growth constants.

6. Summary

Finite element analyses were constructed to independently study the relative effects of silicon particle size, shape, spacing, configuration, alignment, grouping, and microporosity on particle fracture and debonding within an Al–1%Si matrix. The meshes were designed to conform to a two-level DOE methodology where the maximum and minimum values for the above seven parameters were determined based on micrographs of a modified cast Al–Si alloy. Particles within some meshes were fractured and debonded a priori in order to study the effects of damaged neighboring particles on the stress distributions near intact particles. The maximum principal stress in the silicon particle was used as a measure of the propensity of a silicon particle to fracture. The maximum hydrostatic stress at the interface between the silicon particle and the Al–1%Si matrix was used as a measure of the propensity of a silicon particle to debond.

Regardless of the damaged state of the neighboring silicon particles, the relative size, grouping, and Al–1%Si matrix microporosity were found to have a negligible effect on the fracture and debonding of intact particles. When all of the silicon particles were intact, the particle shape and alignment were the only parameters among those considered which significantly affected the fracture and debonding of silicon particles within the Al–1%Si matrix. Intact elliptical particles demonstrated the most resistance to fracture and debonding when the major axis of the particle was perpendicular to the applied loading direction. When the major axis of an elliptical particle was parallel to the applied loading direction, the elongated particle demonstrated the least resistance to particle fracture and debonding. Circular particles demonstrated a resistance to fracture and debonding bounded by elliptical particles of the two orientations mentioned above.

When a crack was introduced through the center of a silicon particle, the fractured particle carried a significant fraction of the local redistributed stress field. The Al–1%Si matrix near the fractured silicon particle experienced only a small localization of stresses near the crack tip. When the lower half of a silicon particle was debonded, the debonded particle carried a negligible fraction of the local stress field. The Al–1%Si matrix near the debonded silicon particle experienced severe localization of stresses over a significant distance from the particle. The localization of stress near the fractured and debonded particles altered the stresses in the adjacent intact particles and along their interfaces depending on the shape and orientation of the damaged particle. Despite the lower stresses in the intact case, fractured and debonded particles with a major axis perpendicular to the loading axis caused a more severe localization of stresses in the surrounding Al–1%Si matrix and the adjacent particles. Furthermore, intact silicon particles placed at a 45° angle, or along a direction perpendicular to the applied loading axis, showed the greatest influence from fractured or debonded particles.

Acknowledgements

This work has been sponsored by the US Department of Energy, Sandia National Laboratories under contract DE-AC04-94AL85000. This work was performed under the leadership of Dick Osborne and Don Penrod for the USCAR Lightweight Metals Group. Mr. Matthew Botos is thanked for his help in constructing some of the finite element meshes.

Appendix A. Design of experiments calculations

The completion of the test matrix in Table 1 yields 16 output values chosen from individual finite element analysis (Table 2). These output values are denoted as O_i , ($i = 1, 2, 3, \dots, 16$), and may represent the maximum principal stress in the particle or hydrostatic pressure at the particle–matrix interface. In a full factorial design, the main parameter effects (E_1 – E_7) and interaction effects (E_{12} , E_{25} , E_{123} , etc.) can be explicitly calculated from the set of O_i values. However, in this fractional factorial design (DeVor et al., 1992), the values calculated directly from the O_i values represent linear combinations of confounded effects (L_1 – L_{16}). The L_i values are calculated through the following relationship (DeVor et al., 1992):

$$\begin{pmatrix} 2L_1 \\ L_2 \\ L_3 \\ L_4 \\ L_5 \\ L_6 \\ L_7 \\ L_8 \\ L_9 \\ L_{10} \\ L_{11} \\ L_{12} \\ L_{13} \\ L_{14} \\ L_{15} \\ L_{16} \end{pmatrix} = \frac{1}{8} \begin{pmatrix} +1 & +1 & +1 & +1 & +1 & +1 & +1 & +1 & +1 & +1 & +1 & +1 & +1 & +1 & +1 & +1 \\ -1 & +1 & -1 & +1 & -1 & +1 & -1 & +1 & -1 & +1 & -1 & +1 & -1 & +1 & -1 & +1 \\ -1 & -1 & +1 & +1 & -1 & -1 & +1 & +1 & -1 & -1 & +1 & +1 & -1 & -1 & +1 & +1 \\ -1 & -1 & -1 & -1 & +1 & +1 & +1 & +1 & -1 & -1 & -1 & -1 & +1 & +1 & +1 & +1 \\ -1 & -1 & -1 & -1 & -1 & -1 & -1 & -1 & +1 & +1 & +1 & +1 & +1 & +1 & +1 & +1 \\ +1 & -1 & -1 & +1 & +1 & -1 & -1 & +1 & +1 & -1 & -1 & +1 & -1 & -1 & +1 & +1 \\ +1 & -1 & +1 & -1 & -1 & +1 & -1 & +1 & -1 & -1 & +1 & -1 & +1 & -1 & +1 & -1 \\ +1 & +1 & -1 & -1 & -1 & -1 & +1 & +1 & +1 & +1 & -1 & -1 & -1 & -1 & +1 & +1 \\ +1 & +1 & -1 & -1 & +1 & +1 & -1 & -1 & -1 & -1 & +1 & +1 & -1 & -1 & +1 & +1 \\ +1 & +1 & +1 & +1 & -1 & -1 & -1 & -1 & -1 & -1 & -1 & -1 & +1 & +1 & +1 & +1 \\ -1 & +1 & +1 & -1 & +1 & -1 & -1 & +1 & -1 & +1 & -1 & +1 & -1 & +1 & -1 & +1 \\ -1 & +1 & +1 & -1 & -1 & -1 & +1 & +1 & -1 & +1 & -1 & +1 & -1 & +1 & -1 & +1 \\ -1 & +1 & -1 & +1 & +1 & -1 & +1 & -1 & -1 & +1 & -1 & +1 & -1 & +1 & -1 & +1 \\ -1 & -1 & +1 & +1 & +1 & +1 & -1 & -1 & +1 & +1 & -1 & -1 & -1 & -1 & +1 & +1 \\ +1 & -1 & -1 & +1 & -1 & +1 & +1 & +1 & -1 & -1 & +1 & +1 & -1 & +1 & -1 & +1 \end{pmatrix} \begin{pmatrix} O_1 \\ O_2 \\ O_3 \\ O_4 \\ O_5 \\ O_6 \\ O_7 \\ O_8 \\ O_9 \\ O_{10} \\ O_{11} \\ O_{12} \\ O_{13} \\ O_{14} \\ O_{15} \\ O_{16} \end{pmatrix}$$

The relationships between the L_i values and the main parameter effects (E_1 – E_7) and interaction effects (E_{12} , E_{25} , E_{123} , etc.) are determined through a confounding relationship. For this common design, the confounding relationship is given in DeVor et al. (1992). It will also be noted that for the present study, three factor interaction effects were ignored which is an accurate assumption for most physically based systems (DeVor et al., 1992). Using the confounding relationship in DeVor et al. (1992), the following equations were determined which relate L_i values to the E values of interest for the present study:

- $L_1 = \text{Data-set mean,}$
- $L_2 = E_1,$
- $L_3 = E_2,$
- $L_4 = E_3,$
- $L_5 = E_4,$
- $L_6 = E_{12} + E_{35} + E_{67},$
- $L_7 = E_{13} + E_{25} + E_{46},$

$$L_8 = E_{14} + E_{36} + E_{57},$$

$$L_9 = E_{23} + E_{15} + E_{47},$$

$$L_{10} = E_{24} + E_{37} + E_{56},$$

$$L_{11} = E_{34} + E_{16} + E_{27},$$

$$L_{12} = E_5,$$

$$L_{13} = \text{Three factor assumption error},$$

$$L_{14} = E_6,$$

$$L_{15} = E_7,$$

$$L_{16} = E_{45} + E_{26} + E_{17}.$$

Hence, given the 16 output values for the meshes in Table 1, the present analysis delivers the seven main parameter effects and the 21 confounded two factor interactions on a chosen output parameter. The main effects (E_1 – E_7) were only considered in this study since the interaction effects were all negligible or obvious from a physical standpoint. For example, a large interaction between particle shape and alignment was uncovered. An interaction between shape and alignment is consistent with expectations since round particles demonstrate no alignment effects, however, elliptical particles demonstrate significant alignment effects.

References

- Hibbitt, Karlsson, & Sorensen, Inc., 1994. ABAQUS/Standard User Manual, vol. 1–6. Hibbitt, Karlsson, & Sorensen, Inc., USA.
- Bammann, D.J., Chiesa, M.L., Horstemeyer, M.F., Weingarten, L.I., 1993. Failure in ductile materials using finite element methods. In: Jones, N., Weirzbicki, T. (Eds.), *Structural Crashworthiness and Failure*. Elsevier Applied Science, Berlin, p. 1 (Chapter 1).
- Bammann, D.J., Chiesa, M.L., Johnson, G.C., 1996. Modeling large deformation and failure in manufacturing processes. In: Tatsumi, Wannabe, Kambe (Eds.), *Theoret. Appl. Mech.* Elsevier Applied Science, Berlin, p. 259.
- Broek, D., 1969. The effect of intermetallic particles on fatigue crack propagation in aluminum alloys. In: Pratt, P.L. (Ed.), *Fracture*, p. 734.
- Broek, D., 1973. The role of inclusions in ductile fracture and fracture toughness. *Engrg. Fract. Mech.* 5, 55.
- Caceres, C.H., Davidson, C.J., Griffiths, J.R., 1995. The deformation and fracture behavior of an Al–Si–Mg casting alloy. *Mater. Sci. Engrg. A* 197, 171.
- Cocks, A.C.F., Ashby, M.F., 1980. Intergranular fracture during power law creep under multiaxial stresses. *Metal Sci.*, 453.
- Cox, T.B., Low Jr., J.R., 1974. *Metall. Trans.* 5, 1457.
- Closset, B., Gruzleski, J.E., 1982. Mechanical properties of A356.0 alloys modified with pure strontium. *AFS Trans.* 90, 453.
- Davidson, D.L., Lankford, J.L., 1985. The effects of aluminum alloy microstructure on fatigue crack growth. *Mater. Sci. Engrg.* 74, 189.
- DeVor, R.E., Chang, T., Sutherland, J.W., 1992. *Statistical Quality Design and Control: Contemporary Concepts and Methods*, First ed. Macmillan, New York.
- Dighe, M.D., Gokhale, A.M., 1997. Relationship between microstructural extremum and fracture path in a cast Al–Si–Mg alloy. *Scr. Metall.* 37, 1435.
- Eshelby, J.D., 1957. The elastic field outside an elliptical inclusion. *Proc. Roy. Soc. London A* 252, 561.
- Gall, K., Yang, N., Horstemeyer, M.F., McDowell, D.L., Fan, J.H., 1999a. The Influence of modified intermetallics and Si particles on fatigue crack paths in a cast A356 Al alloy. *Fat. Frac. Engrg. Mat. Struc.* (in press).
- Gall, K., Yang, N., Horstemeyer, M.F., McDowell, D.L., Fan, J.H., 1999b. The debonding and fracture of Si particles during the fatigue of a cast Al–Si alloy. *Metall. Trans. A* 30, 3078–3088.
- Garrison, W.M., Moody, N.R., 1987. Ductile fracture. *J. Phys. Chem. Solids* 48, 1035.
- Gurland, J., Plateau, J., 1963. The mechanism of ductile rupture of metals containing inclusions. *Trans. ASM* 56, 442.
- Hahn, G.T., Rosenfield, A.R., 1975. Metallurgical factors affecting fracture toughness of aluminum alloys. *Metall. Trans. A* 6, 653.
- Horstemeyer, M.F., 1998. Damage influence on Bauschinger effect of a cast A356 aluminum alloy. *Scr. Mater.* 39, 1491.
- Hoskin, G.A., Provan, J.W., Gruzleski, J.E., 1988. The in-situ fatigue testing of a cast aluminum–silicon alloy. *Theoret. Appl. Frac. Mech.* 10, 27.

- Kearney, A., Rooy, E.L., 1990. Aluminum foundry products. ASM Handbook 2, 123.
- Lee, F.T., Major, J.F., Samuel, F.H., 1995a. Fracture behavior of Al12wt% Si0.35wt% Mg(0-0.02)wt% Sr castings under fatigue testing. *Fat. Frac. Engrg. Mat. Struct.* 18, 385–396.
- Lee, F.T., Major, J.F., Samuel, F.H., 1995b. Effect of silicon particles on the fatigue crack growth characteristics of Al–12 Wt Pct Si–0.35 Wt Pct Mg–(0 to 0.02) Wt Pct Sr casting alloys. *Metall. Mater. Trans. A* 26, 1553.
- Murali, S., Trivedi, A., Shamanna, K.S., Murthy, K.S.S., 1996. Effect of iron and combined iron and beryllium additions on the fracture toughness and microstructures of squeeze cast Al–7Si–0.3Mg alloy. *J. Mater. Engrg. Perform.* 5, 462.
- Needleman, A., 1987. A continuum model for void nucleation by inclusion debonding. *J. Appl. Mech.* 109, 525.
- Pan, E.N., Chiou, H.S., Laio, G.J., 1991. Effects of modification and solidification conditions on the feeding behavior of A356 aluminum alloy. *AFS Trans.* 99, 605.
- Plumtree, A., Schafer, S., 1986. Initiation and short crack behavior in aluminum alloy castings. In: Miller, K.J., de los Rios, E.R. (Eds.), *The Mechanical Behavior of Short Fatigue Cracks*. EGF Publication 1, Suffolk, UK, p. 215.
- Samuel, A.M., Samuel, F.H., 1995. A metallographic study of porosity and fracture behavior in relation to the tensile properties in 319.2 end chill castings. *Metall. Mater. Trans. A* 26, 2359.
- Shiozawa, K., Tohda, Y., Sun, S-M., 1997. Crack initiation and small fatigue crack growth behavior of squeeze-cast Al–Si aluminum alloys. *Fat. Frac. Engrg. Mat. Struc.* 20, 237.
- Tan, Y.H., Lee, S.L., Lin, Y.L., 1995. Effects of Be and Fe content on plane strain fracture toughness in A357 alloys. *Metall. Mater. Trans. A* 26, 2937.
- Ting, J.C., Lawrence, F.V., 1993. Modeling the long-life fatigue behavior of a cast aluminum alloy. *Fat. Frac. Engrg. Mat. Struc.* 16, 631.
- Voigt, R.C., Bye, D.R., 1991. Microstructural aspects of fracture in A356. *AFS Trans.* 99, 33.
- Yeh, J.-W., Liu, W.-P., 1996. The cracking mechanism of silicon particles in an A357 aluminum alloy. *Metall. Mater. Trans. A* 27, 3558.